Nuclear Engineering and Technology 54 (2022) 3140–3153

Contents lists available at ScienceDirect

Nuclear Engineering and Technology

journal homepage: www.elsevier.com/locate/net

Original Article

# Numerical investigation of a plate-type steam generator for a small modular nuclear reactor

Jinhoon Kang [a], Jin-Yeong Bak [a], Byung Jin Lee [b], Chang Kyu Chung [b], Byongjo Yun [a, *]

[a] School of Mechanical Engineering, Pusan National University, Busan, 46241, Republic of Korea
[b] KEPCO Engineering & Construction, Daejeon, 34057, Republic of Korea

ARTICLE INFO

*Article history:*
Received 22 November 2021
Received in revised form
20 January 2022
Accepted 19 February 2022
Available online 23 February 2022

*Keywords:*
Steam generator
Corrugated plate
Boiling
Reverse gradient
Ledinegg instability

ABSTRACT

A numerical feasibility study was conducted to investigate the thermal–hydraulic characteristics of a steam generator with corrugated plates for a small modular reactor. Accordingly, a one-dimensional thermal–hydraulic analysis code was developed based on the existing state-of-the-art thermal–hydraulic models and correlations for corrugated plate heat exchangers. Subsequently, the pressure loss, heat transfer, and instability characteristics of the steam generator with corrugated plates were investigated according to the chevron angle and mass flux. Additionally, the characteristics of rectangular and disk-type corrugated plate steam generators with equivalent heat transfer areas were analyzed. The steam generator with disk-type corrugated plates exhibited better performance in terms of pressure loss and heat transfer rate than the rectangular type. In addition, when the mass flux decreased from the onset of boiling points, reverse gradients of the total pressure change were observed in both types. Thus, it was confirmed that Ledinegg instability could occur in the steam generator with corrugated plates. However, it was dependent on the chevron angle, and the optimal chevron angle to minimize instability was 45° under the conditions of the present analysis.



## 1. Introduction

Corrugated plate heat exchangers (CPHEs) are widely used in various industries, such as air conditioning equipment, shipbuilding, chemical plants, and power plants because of their high heat transfer performance and compactness. They are manufactured by stacking corrugated plates, and the working fluid is passed through the channel between two adjacent plates. However, a highly turbulent flow is generated in the CPHE channels despite the low Reynolds number conditions owing to the complicated channel geometry. Therefore, the CPHE has a high heat transfer performance compared with other heat exchanger types, such as shell-and-tube heat exchangers. Furthermore, CPHE provides a large heat transfer area per unit volume because of the corrugations on the heat transfer surface.

Recently, various small modular reactors (SMRs) have been developed worldwide for carbon-free electricity production. SMRs require innovatively designed small components with high performance. However, the shell-and-tube steam generators (SGs) used in conventional pressurized water reactors (PWRs) are large, making the design of integrated SMRs difficult. Thus, it is necessary to design compact SGs to support the development of SMRs. The CPHE, which has a small volume and high heat transfer performance, is a promising candidate for replacing conventional SGs. Therefore, feasibility studies are necessary to determine the heat transfer and pressure loss characteristics of the CPHE SG.

Many previous experimental studies have been performed for rectangular-type CPHE. In the experiments, the heat transfer rate and pressure loss data were collected by measuring the temperature and pressure at the inlet or outlet of the CPHE. Muley and Manglik [1] performed experiments on the heat transfer and pressure loss in a single-phase flow. They used three rectangular CPHEs with different chevron angles to investigate the chevron angle effect. Gulenoglu et al. [2] conducted an experimental study by varying the mass flux and fluid temperature. Kumar [3] and Thonon [4] proposed heat transfer and pressure loss correlations for a CPHE under single-phase flow based on their respective experimental data.

Additionally, boiling flow experiments were conducted using rectangular CPHEs. Han et al. [5] and Khan et al. [6–8] performed experiments to observe the effect of the chevron angle on the

* Corresponding author.
*E-mail address:* bjyun@pusan.ac.kr (B. Yun).

https://doi.org/10.1016/j.net.2022.02.020

boiling heat transfer and pressure loss using R410a and ammonia as working fluids, respectively. Yan et al. [9] and Hsieh et al. [10] investigated the refrigerant heat transfer and pressure loss behaviors in the boiling regions for heat flux, mass flux, and pressure.

Analytical studies were also performed to investigate the local phenomena predicted in the CPHE. Tsai et al. [11] explored the pressure loss and flow rate differences between the channels of CPHE in a single-phase flow using CFD analysis. The analysis simulated two channels consisting of a rectangular CPHE and water flow without heat transfer between the two channels. The differences in the pressure loss and flow rate between the two channels were 0.28% and 0.8%, respectively, demonstrating that the working fluid was uniformly distributed in each CPHE channel. Han et al. [12] performed a CFD calculation for the heat transfer of subcooled water in a rectangular CPHE. They examined local thermal–hydraulic parameters, such as fluid temperature, velocity, and pressure. They reported that the velocity was almost zero around the inlet and outlet, and the heat transfer rate at these points was much lower than that in the other areas. In addition, the pressure changed mainly along the flow direction. Yoon et al. [13] developed a network model to analyze single-phase and condensation flows in rectangular CPHEs. The network model was based on empirical correlations for the heat transfer coefficient and wall friction factor as proposed in previous studies. They compared the results predicted by the network model with their experimental data for refrigerants. This study demonstrated that the empirical correlation is useful for the analysis of local thermal–hydraulic characteristics.

Research was conducted on CPHE SGs in naval PWRs [14]. However, the performance of CPHE SGs in commercial nuclear power plants has never been evaluated. Furthermore, limited studies on disk CPHEs have been conducted with most previous studies being conducted for rectangular CPHEs. To address this gap, a one-dimensional code to analyze the thermal–hydraulic characteristics of CPHE SGs was developed in this study. A feasibility analysis of the CPHE SGs was then performed for SMR. The analysis evaluated the performances of both rectangular and disk-type CPHEs using the developed code.

## 2. 1-D thermal–hydraulic analysis code

In the study of the CPHE as a SG, BANDI-60 SMR [15], which was developed by KEPCO E&C, was chosen as a reference plant. Herein, water with a pressure of 15 MPa and a temperature of 325 °C flows to the primary side of the SG, and water at a temperature of 232.2 °C is injected into the secondary side as feedwater. Water in the secondary side is expected to evaporate due to heat transfer from the primary side and become saturated steam. The pressure at the outlet of the secondary side was 6 MPa, and the code for evaluating the CPHE SGs under the expected BANDI-60 operating conditions was developed in this study.

### 2.1. Geometry of CPHE type SG

The CPHE is classified as rectangular and disk-type CPHE according to the shape of the corrugated plates. The rectangular CPHE consists of narrow and long plates, as shown in Fig. 1 (a), and it is manufactured by stacking corrugated plates without external casings. The primary and secondary working fluids were injected and discharged through the inlet and outlet located at the top and bottom of the plates, respectively. The channels along the primary and secondary sides were physically separated by the corrugated plates. The primary fluid at a high temperature was injected into the inlet located at the top. This fluid flowed downward, whereas the secondary fluid flowed in the opposite direction as that of the primary fluid.

The disk CPHE consists of an assembly of disk plates in a cylindrical container, as shown in Fig. 1 (b). The main flow directions in the disk CPHE were the same as those in the rectangular CPHE. However, unlike the rectangular CPHE, the flow cross-sectional area of the disk CPHE changes along the main flow direction.

The corrugations of both CPHEs were assumed to have equal intervals along the flow direction, as shown in Fig. 2. The angle between the corrugation and vertical axis significantly affects the CPHE performance and is defined as the chevron angle ($\beta$). $L$ represents the distance between the inlet and the outlet.

The corrugation shape of typical CPHEs is sinusoidal, and the flow channels between these plates are formed as shown in Fig. 3. The hydraulic diameter ($d_h$) of the flow channel is calculated as follows:

$$d_h = \frac{2b}{\phi}, \tag{1}$$

where $b$ is the corrugation height, and $\phi$ is the enlargement factor [13]. The enlargement factor represents the ratio of the actual heat transfer area to the projected area.

$$\phi \cong \frac{1}{6}\left(1+\sqrt{1+\left(\frac{\pi b}{\lambda}\right)^2}+4\sqrt{1+\left(\frac{\pi b}{\lambda}\right)^2\Big/2}\right), \tag{2}$$

where $\lambda$ is the pitch of the corrugation plate.

The average flow cross-sectional area ($A_{cs}$) affecting the performances of the CPHEs depends on the width of CPHE ($W$) and the height of corrugation. In rectangular CPHE, the width of CPHE does not change along the axial direction. Thus, the average flow cross-sectional area of rectangular CPHE is constant as follows:

$$A_{CSRect} = bW_{Rect}. \tag{3}$$

However, the width of disk CPHE changes along the axial direction. Therefore, the average width of disk CPHE ($\overline{W}_{disk}$) at a given elevation in the region between inlet and outlet can be expressed as follows:

$$\overline{W}_{disk} = 4\left(\frac{d_{disk}}{2}\right)^2\left(\frac{1}{2}\left(\sin^{-1}\frac{L}{d_{disk}}\right)+\frac{1}{4}\sin\left(2\sin^{-1}\frac{L}{d_{disk}}\right)\right)\Big/ L, \tag{4}$$

where $d_{disk}$ and $L$ are the diameter of the disk plate and the distance between inlet and outlet, respectively. The average flow cross-sectional area of disk CPHE is calculated as follows:

$$\overline{A_{CS}}_{disk} = b\overline{W}_{disk}. \tag{5}$$

### 2.2. Development of 1-D thermal-hydraulic analysis code

A one-dimensional thermal-hydraulic analysis code was developed to evaluate the performance of the rectangular and disk-type CPHE SGs. The calculation nodes of the primary and secondary sides were constructed along the flow direction, as shown in Fig. 4. The nodes were modeled to reflect changes in the channel cross-sectional area along the axial flow direction.

Accordingly, the flow cross-sectional area and the heat transfer area of each node are determined as follows:

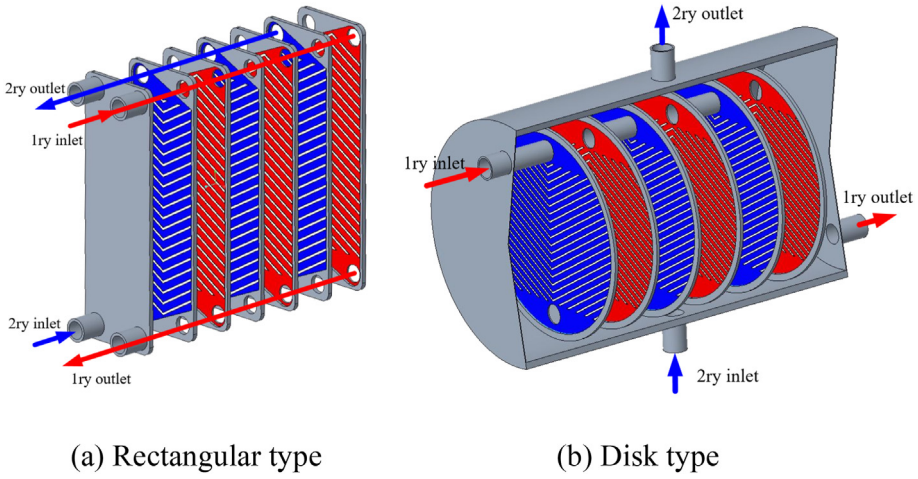


**Fig. 1.** Arrangement of plates for CPHEs.

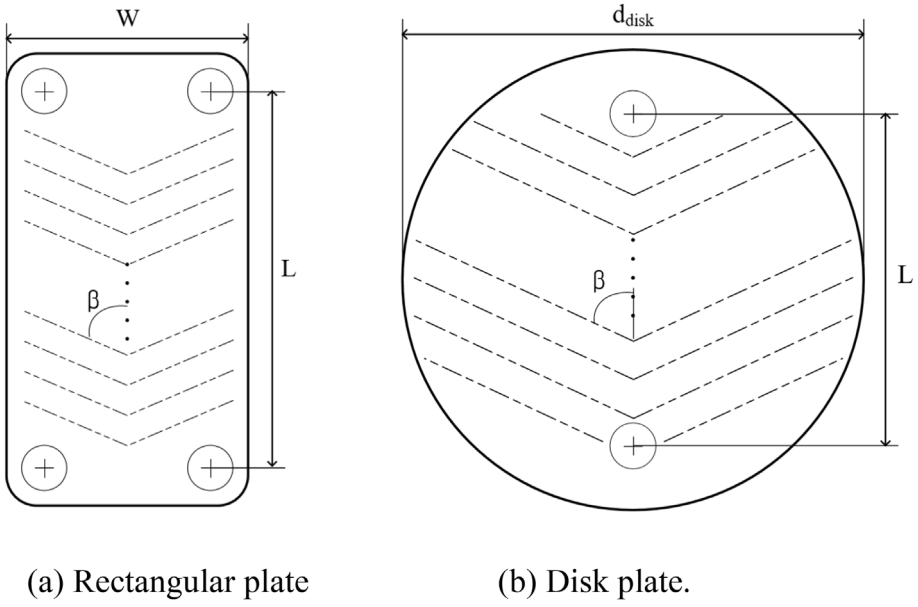


**Fig. 2.** Shape of corrugated plates.

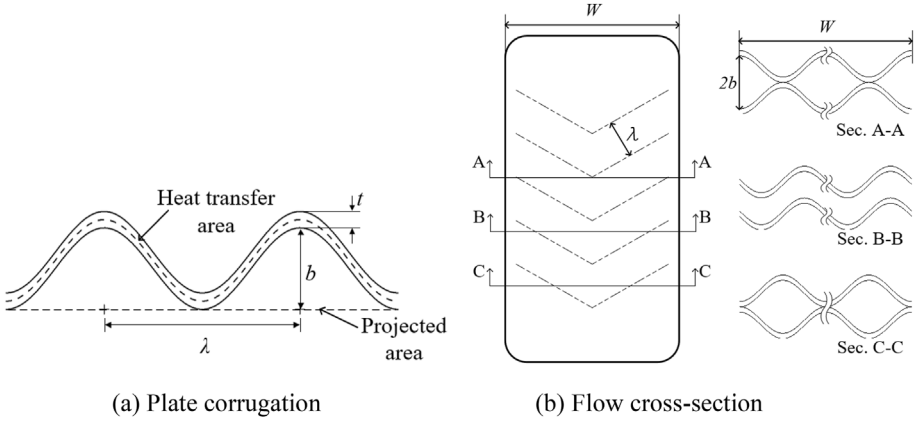


**Fig. 3.** Geometrical design of corrugated plate.

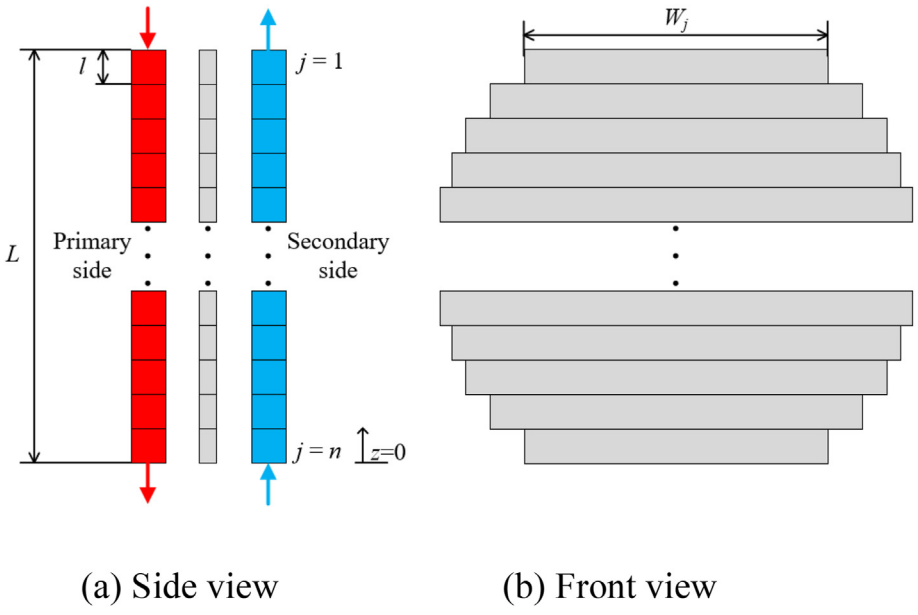


**Fig. 4.** Nodalization for disk CPHE.

$$A_{CS,j} = bW_j, \tag{6}$$

$$A_{HT,j} = 2lW_j, \tag{7}$$

where $W_j$ and $l$ are the width of $j$th node and the axial node size.

To calculate the thermal–hydraulic parameters in the flow channels, a one-dimensional code was developed based on the mass, momentum, and energy governing equations for single- and two-phase flows as follows:

$$\frac{\partial \rho}{\partial t} + \frac{1}{A_{CS}} \frac{\partial}{\partial z}(\rho u A_{CS}) = 0, \tag{8}$$

$$\frac{\partial}{\partial t}(\rho u) + \frac{1}{A_{CS}} \frac{\partial}{\partial z}\left(\rho u^2 A_{CS}\right) = -\frac{\partial P_s}{\partial z} - \rho g - F_w, \tag{9}$$

$$\frac{\partial}{\partial t}(\rho i) + \frac{1}{A_{CS}} \frac{\partial}{\partial z}(\rho u A_{CS} i) = \frac{1}{A_{CS}} \frac{\partial}{\partial z}(q'' A_{HT}) + \dot{q}, \tag{10}$$

where $\rho$, $u$, $i$, $z$, $q''$, and $\dot{q}$ are the fluid density, velocity, enthalpy, flow direction, heat flux, and heat generation rate, respectively. In these formulations, the two-phase flow was considered to be a homogeneous mixture. Thus, the fluid mixture density ($\rho_m$) and enthalpy ($i_m$) in the two-phase flow condition were calculated based on the thermodynamic quality ($x$) as follows:

$$\rho_m = \left(\frac{1-x}{\rho_f} + \frac{x}{\rho_g}\right)^{-1}, \tag{11}$$

$$i_m = (1-x) i_f + x i_g, \tag{12}$$

The analysis is intended for the SG in the steady-state flow conditions without internal heat generation; therefore, the governing equations for nodes were recast as follows:

$$G_{j+1} A_{CS,j+1} = G_j A_{CS,j}, \tag{13}$$

$$P_{j+1} + \frac{G_{j+1}^2}{2\rho_{j+1}} + \rho_{j+1} g z_{j+1} = P_j + \frac{G_j^2}{2\rho_j} + \rho_j g z_j - \Delta P_{loss,j} \tag{14}$$

$$G_{j+1} A_{CS,j+1} i_{j+1} - G_j A_{CS,j} i_j = h_j A_{HT,j} (T_{w,j} - T_j) \tag{15}$$

where $G$, $P$, $h$, $T$, and $T_w$ are the mass flux, pressure, heat transfer coefficient, fluid temperature, and wall temperature, respectively. The $\Delta P_{loss,j}$ in Eq. (12) represents the irreversible frictional or form loss of a single or two-phase flow at the $j$th node, and it is calculated as follows:

$$\Delta P_{loss,j} = 4 f_j \frac{l}{d_h} \frac{G_j^2}{2\rho_j} + K \frac{G_j^2}{2\rho_j} \left(1 + x_j \left(\frac{\rho_f}{\rho_g} - 1\right)\right) \tag{16}$$

where $f$ is the wall friction factor. In previous studies [1–4], the wall friction factor was derived from the pressure loss caused by the corrugation plate in the CPHE. In addition, for the disk CPHE, because the channel cross-sectional area along the flow direction changed, pressure loss due to the change in the flow area was also expected. To consider this pressure loss, the following form loss coefficient, $K$ [14], was applied:

Contraction

$$K = \left(\frac{1 - A_{CS,small}/A_{CS,large}}{1.08\left(1 - A_{CS,small}/A_{CS,large}\right) + 0.5371}\right)^2 \tag{17}$$

Expansion

$$K = \left(1 - \left(\frac{A_{CS,small}}{A_{CS,large}}\right)^2\right)^2 \tag{18}$$

where $A_{CS,small}$ and $A_{CS,large}$ are the flow cross-sectional areas in the point where the flow cross-sectional areas of adjacent nodes change.

### 2.3. Constitutive models and correlations

To calculate the thermal–hydraulic parameters with the one-dimensional governing equations, models and correlations for the single-phase, as well as boiling heat transfer coefficients and wall friction factors should be provided. In this study, these were determined based on evaluating the models and correlations available from open literature experimental data to apply to the one-dimensional analysis code.

#### 2.3.1. Single-phase flow region

The correlations of the heat transfer coefficient and wall friction factor in the single-phase flow for CPHE have been proposed by several researchers. Among them, the correlations proposed by Muley and Manglik [1], Kumar [3], and Thonon [4] were evaluated because they consider the effect of the chevron angle. The correlations were formulated using the Reynolds number ($\mathrm{Re} = \mathrm{G}d_h/\mu$) and Prandtl number ($\mathrm{Pr} = c_p\mu/k$), as shown in Table 1. The $\mu$ and $\mu_w$ are the viscosities calculated at the fluid temperature and wall temperature, respectively.

Muley and Manglik developed correlations between the heat transfer coefficient and wall friction factor using experimental data produced by three rectangular CPHEs with different chevron angles. The correlations consider the effects of geometric parameters, such as the chevron angle and enlargement factor. The Reynolds number coverage of the correlations was $6 \times 10^2$–$10^4$. Kumar and Thonon proposed correlations using different coefficients depending on the chevron angle and Reynolds number with experimental data: the working fluid was water. The applicable ranges of the correlations are $Re \leq 10^4$ and $50 \leq \mathrm{Re} \leq 1.5 \times 10^4$, respectively.

To evaluate the correlations for single-phase flow, Muley and Manglik [1] data and Gulenoglu et al. [2] data were collected to establish an experimental database. Muley and Manglik measured the heat transfer rate and pressure loss in rectangular CPHEs with chevron angles of 30°, 45°, and 60° under the conditions of Reynolds numbers ranging from $6 \times 10^2$ to $10^4$. Gulenoglu et al. performed experiments in a rectangular CPHE with a chevron angle of 60°. In the experiment, water was used as the working fluid, and the Reynolds number was in the range of $3 \times 10^2$–$5 \times 10^3$. The CPHE geometry and flow conditions for both experiments are summarized in Table 2.

The aforementioned three correlations for single-phase flow were evaluated against the experimental database, and their prediction performances were quantified using the root mean square error (RMSE) defined below:

$$RMSE = \sqrt{\frac{1}{N}\sum\left(\frac{X_{calculated} - X_{Exp.}}{X_{Exp.}}\right)^2}, \tag{19}$$

The evaluation results of the heat transfer correlations are shown in Fig. 5. The Muley and Manglik correlation predicted most of the experimental data within an error of 20%. On the other hand, Kumar correlation underestimated Muley and Manglik's data with a chevron angle of 30° by 10% and overestimated the other data for the different chevron angles by 35%. The Thonon correlation is in

**Table 1**
Correlations for single-phase heat transfer and wall friction factor.

| Author | Correlation | | | | | Applicable range | |
|---|---|---|---|---|---|---|---|
| Muley and Manglik [1] | $Nu = [0.2668 - 0.006967\beta + 7.244\times10^{-5}\beta^2] \times [20.78 - 50.94\varnothing + 41.16\varnothing^2 - 10.51\varnothing^3] \times Re^{[0.728+0.0543\sin(\frac{\pi\beta}{45}+2.1)]} Pr^{1/3}(\mu/\mu_w)^{0.14}$<br>$f = [2.917 - 0.1277\beta + 2.016\times10^{-3}\beta^2] \times [5.474 - 19.02\varnothing + 18.93\varnothing^2 - 5.341\varnothing^3] \times Re^{-[0.2+0.0577\sin(\frac{\pi\beta}{45}+2.1)]}$ | | | | | Water<br>$10^3 \leq \mathrm{Re} \leq 10^4$<br>$2 \leq \mathrm{Pr} \leq 6$<br>$30° \leq \beta \leq 60°$ | |
| Kumar [3] | $Nu = C_1 Re^m Pr^{1/3}(\mu/\mu_w)^{0.17}$<br>$f = C_2/Re^p$ | | | | | Water<br>$Re \leq 10^4$ | |
| | $\beta$ | $Re$ | $C_1$ | $m$ | $Re$ | $C_2$ | $p$ |
| | ≤30 | ≤10 | 0.718 | 0.349 | <10 | 50.0 | 1.0 |
| | | >10 | 0.348 | 0.663 | 10–100 | 19.40 | 0.589 |
| | | | | | >100 | 2.990 | 0.183 |
| | 45 | <10 | 0.718 | 0.349 | <15 | 47.0 | 1.0 |
| | | 10–100 | 0.400 | 0.598 | 15–300 | 18.29 | 0.652 |
| | | >100 | 0.300 | 0.633 | >300 | 1.441 | 0.206 |
| | 50 | <20 | 0.630 | 0.333 | <20 | 34.0 | 1.0 |
| | | 20–300 | 0.291 | 0.591 | 20–300 | 11.25 | 0.631 |
| | | >300 | 0.130 | 0.732 | >300 | 0.772 | 0.161 |
| | 60 | <20 | 0.562 | 0.326 | <40 | 24.0 | 1.0 |
| | | 20–400 | 0.306 | 0.529 | 40–400 | 3.24 | 0.457 |
| | | >400 | 0.108 | 0.703 | >400 | 0.760 | 0.215 |
| | ≥65 | <20 | 0.562 | 0.326 | <50 | 24.0 | 1.0 |
| | | 20–500 | 0.331 | 0.503 | 50–500 | 2.80 | 0.451 |
| | | >500 | 0.087 | 0.718 | >500 | 0.639 | 0.213 |
| Thonon [4] | $Nu = C_1 Re^m Pr^{1/3}$<br>$f = C_2/Re^p$ | | | | | Water<br>$50 \leq Re \leq 1.5\times10^4$ | |
| | $\beta$ | $Re$ | $C_1$ | $m$ | $Re$ | $C_2$ | $p$ |
| | 30 | 50–15000 | 0.1000 | 0.687 | ≤1000 | 28.21 | 0.900 |
| | | | | | >1000 | 0.872 | 0.392 |
| | 45 | 50–15000 | 0.2267 | 0.631 | ≤550 | 26.34 | 0.830 |
| | | | | | >550 | 0.572 | 0.217 |
| | 60 | 50–15000 | 0.2998 | 0.645 | ≤200 | 18.19 | 0.682 |
| | | | | | >200 | 0.6857 | 0.172 |
| | 75 | 50–15000 | 0.2946 | 0.700 | ≤160 | 45.57 | 0.670 |
| | | | | | >160 | 0.370 | 0.172 |

**Table 2**
Experimental database for single-phase flow.

| Author | Working fluid | Geometry | Experiment condition |
|---|---|---|---|
| Muley and Manglik [1] | Water | $L$ = 392 mm<br>$W$ = 163 mm<br>$\beta$ = 30, 45, 60° $b$ = 2.5 mm<br>λ = 9 mm | Re = $6 \times 10^2$–$10^4$<br>$Pr$ = 2–6 |
| Gulenoglu et al. [2] | Water | $L$ = 632 mm<br>$W$ = 443 mm<br>$\beta$ = 60° $b$ = 2.64 mm<br>λ = 10 mm | Re = $3 \times 10^2$–$5 \times 10^3$<br>$Pr$ = 1.9–5.7 |

good agreement with Muley and Manglik's 30° data. However, it over-predicted the other data, and the discrepancy increased with the chevron angle. From the evaluation, the Muley and Manglik correlation showed the best prediction capability for the experimental data, as shown in Table 3. Therefore, it was chosen as the heat transfer correlation for single-phase flow.

The evaluation of the wall friction factor correlation in Table 1 was performed, and the results are shown in Fig. 6 and Table 4. The Muley and Manglik correlation predicted all data within an error of 19%. Kumar correlation underestimated Muley Manglik's data for chevron angles of 30° and 45°, whereas it overestimated the other data for a chevron angle of 60°. Thonon correlation greatly under-predicted all experimental data. Thus, the Muley and Manglik correlation was selected as the wall friction factor because it showed the best evaluation results.

### 2.3.2. Boiling region

The available CPHE boiling correlations reflecting the chevron angle effect were surveyed to select the boiling correlations for the SG. Han et al. [5] developed a correlation based on R410a boiling data produced from rectangular CPHEs. It considers the effect of the pitch of the plate corrugation with respect to the geometric parameters on the coefficients as follows:

$$Nu = Ge_1 Re_{eq}^{Ge_2} Bo_{eq}^{0.3} Pr^{0.4}, \tag{20}$$

$$Ge_1 = 2.81\left(\frac{\lambda}{d_h}\right)^{-0.041}\left(\frac{\pi\beta}{180}\right)^{-2.83}, \tag{21}$$

$$Ge_2 = 0.746\left(\frac{\lambda}{d_h}\right)^{-0.082}\left(\frac{\pi\beta}{180}\right)^{0.61}, \tag{22}$$

where $Re_{eq}$ and $Bo_{eq}$ are the Reynolds number ($Re_{eq} = G_{eq}d_h/\mu_f$) and Boiling number ($Bo_{eq} = q/G_{eq}i_{fg}$) for the two-phase flow, respectively. The parameters were defined based on the equivalent mass flux of the two-phase flow:

$$G_{eq} = G\left(1 - x + x\left(\frac{\rho_f}{\rho_g}\right)^{1/2}\right), \tag{23}$$

The pressure loss of the two-phase flow contains the wall friction and interfacial friction between gas and liquid, and they are generally obtained by applying a two-phase multiplication factor to a single-phase flow pressure loss. However, the wall friction factor for the CPHE was developed considering the pressure loss caused by the wall friction and the interfacial friction of the two-phase flow. Han et al. proposed the wall friction factor correlation as a function of $Re_{eq}$, and the geometric effects were reflected by the coefficients:

$$f = Ge_3 Re_{eq}^{Ge_4}, \tag{24}$$

$$Ge_3 = 64,710\left(\frac{\lambda}{d_h}\right)^{-5.27}\left(\frac{\pi\beta}{180}\right)^{-3.03}, \tag{25}$$

$$Ge_4 = -1.314\left(\frac{\lambda}{d_h}\right)^{-0.62}\left(\frac{\pi\beta}{180}\right)^{-0.47}. \tag{26}$$

The applicable ranges are $1.0 \times 10^3 \le Re_{eq} \le 3.4 \times 10^3$, $1.8 \times 10^{-4} \le Bo_{eq} \le 6.0 \times 10^{-4}$, $2.3 \le Pr_f \le 2.34$, and $45° \le \beta \le 70°$.

Khan et al. [6–8] conducted boiling experiments in rectangular CPHEs with ammonia and used the obtained data to develop a heat transfer correlation as follows:

$$Nu = \left(-173.52\frac{\beta}{60} + 257.12\right)\left(Re_{eq}Bo_{eq}\right)^{-0.09\frac{\beta}{60}+0.0005}\left(\frac{P_{sat}}{P_{cr}}\right)^{-0.624\frac{\beta}{60}+0.822}, \tag{27}$$

where $P_{sat}$ is the saturated pressure and $P_{cr}$ is the critical pressure of the working fluid. They also proposed the wall friction factor for each chevron angle as follows:

$$f = 673,336 Re_{eq}^{-1.3}\left(\frac{P_{sat}}{P_{cr}}\right)^{0.9}, \text{ for } \beta = 30° \tag{28}$$

$$f = 305,590 Re_{eq}^{-1.26}\left(\frac{P_{sat}}{P_{cr}}\right)^{0.9}, \text{ for } \beta = 45° \tag{29}$$

$$f = 212 Re_{eq}^{-0.51}\left(\frac{P_{sat}}{P_{cr}}\right)^{0.53}, \text{ for } \beta = 60° \tag{30}$$

The applicable ranges of Khan et al. correlations are $6.3 \times 10^2 \le Re_{eq} \le 1.6 \times 10^3$ and $3.3 \times 10^{-4} \le Bo_{eq} \le 1.1 \times 10^{-3}$.

Amalfi [16,17] used the boiling experimental data from previous studies to investigate the two-phase flow phenomena at the micro- and macroscales according to the Bond number ($Bd = (\rho_f - \rho_g)gd_h^2/\sigma) = 4$ [18]. He developed heat transfer correlations for microscale ($Bd < 4$) and macroscale ($Bd \ge 4$) as follows:

$$Nu = 982\beta^{*1.101} We_m^{0.315} Bo^{0.320} \rho^{*-0.224}, \text{ for } Bd < 4 \tag{31}$$

$$Nu = 18.495\beta^{*0.248} Re_g^{0.135} Re_{fo}^{0.351} Bd^{0.235} Bo^{0.198} \rho^{*-0.223}, \text{ for } Bd \le 4 \tag{32}$$

where $\beta^*$, $We_m$, $Bo$, $\rho^*$, $Re_g$, and $Re_{fo}$ are the chevron angle ratio

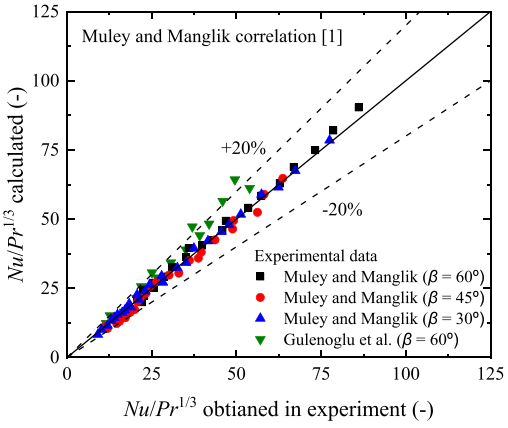


(a) Muley and Manglik correlation

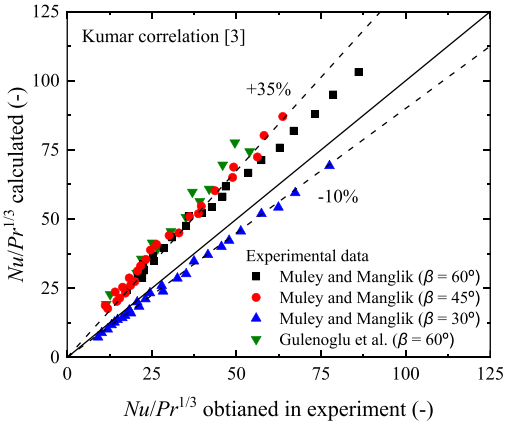


(b) Kumar correlation

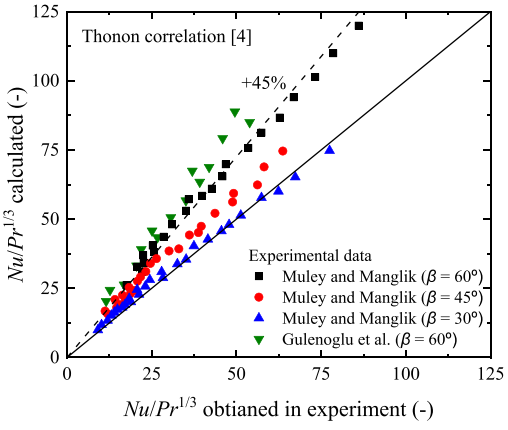


(c) Thonon correlation

**Fig. 5.** Evaluations of correlations for single-phase convection heat transfer.

($\beta^* = \beta/70^\circ$), Weber number ($We_m = G^2 d_h/\rho_m\sigma$), Boiling number ($Bo = q''/Gh_{fg}$), density ratio ($\rho^* = \rho_f/\rho_g$), Reynolds numbers of saturated steam ($Re_g = Gxd_h/\mu_g$), and liquid ($Re_{fo} = Gd_h/\mu_f$), respectively.

Amalfi also proposed the correlation for wall friction factor as follows:

**Table 3**
RMSE of the correlations for single-phase convection heat transfer.

| | RMSE (−) | | |
|---|---|---|---|
| Experiments | Muley and Manglik | Kumar | Thonon |
| Muley and Manglik ($\beta = 60^\circ$) | 0.047 | 0.335 | 0.483 |
| Muley and Manglik ($\beta = 45^\circ$) | 0.079 | 0.456 | 0.284 |
| Muley and Manglik ($\beta = 30^\circ$) | 0.040 | 0.117 | 0.101 |
| Gulenoglu et al. ($\beta = 60^\circ$) | 0.169 | 0.548 | 0.710 |
| Total | 0.087 | 0.376 | 0.409 |

$$f = \left(2.125\beta^{*9.993} + 0.955\right) 15.698 We_m^{-0.475} Bd^{0.255} \rho^{*-0.571}. \quad (33)$$

The applicable ranges of Amalfi correlations for heat transfer and friction factor are listed in Table 5.

An experimental database for the CPHE is necessary for evaluating the above correlations for the boiling flow. Thus, the experimental data by Hsieh et al. [10], Yan et al. [9], Khan et al. [6–8], and Han et al. [5] were collected. Hsieh et al. and Yan et al. performed boiling experiments on refrigerants R410a and R134a, respectively, using rectangular CPHE with a chevron angle of 60°. The heat transfer rate and pressure loss data were produced by changing the mass flux, heat flux, and pressure in the experiments. Han et al. investigated the chevron angle effect in rectangular CPHEs with 45°, 55°, and 70° under the R410a boiling condition. Khan et al. used three rectangular CPHEs with chevron angles of 30°, 45°, and 60° and conducted experiments under one mass flux condition per chevron angle. The working fluid in the experiments conducted by Khan et al. was ammonia. The experimental conditions used in these experiments are listed in Table 6.

The evaluation results of the boiling heat transfer correlations proposed by Han et al. Khan et al., and Amalfi are presented in Fig. 7 and Table 7. Han et al. correlation predicted their data within a RMSE of 0.125. However, it underestimated the data of Hsieh et al. and Yan et al. by 30% and overestimated the data of Khan et al. by 45%. The correlation proposed by Khan et al. reasonably predicted their data. However, it did not follow the tendencies of other data. The RMSE of the Amalfi correlation for the dataset was 0.235, which is the smallest error among the correlations. Therefore, the Amalfi correlation was adopted as the boiling heat transfer correlation for the one-dimensional analysis code.

The predictive performances of the wall friction factor correlations in boiling were compared. The results are shown in Fig. 8 and Table 8. The correlation proposed by Han et al. underestimated the data of Hsieh et al. and Yan et al. whereas it overestimated Khan et al.'s data as in the heat transfer case. Khan et al. correlation under-predicted Hsieh et al. and Yan et al.'s data, and the prediction results of Han et al.'s data were significantly scattered. The Amalfi correlation predicted most of the data to be within 40%. Therefore, Amalfi's wall friction factor was chosen as the boiling region.

### 2.4. Code validation

The developed code was validated against the existing experimental data. The data on heat transfer rate obtained from Hsieh et al. [10], Han et al. [5], and Yan et al. [9]'s experiments on boiling were used for the validation. The heat transfer rate obtained in the experiment ($Q_{experiment}$) and calculated ($Q_{calcualted}$) using the code with respect to the quality is shown in Fig. 9. The developed code predicted most of the data within 25% error. The error range corresponds to the uncertainty of the Amalfi correlation, which is

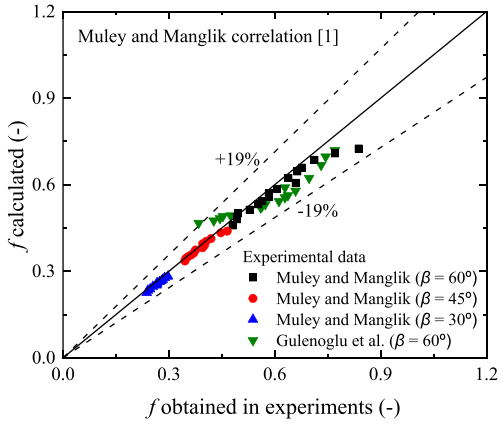


(a) Muley and Manglik correlation

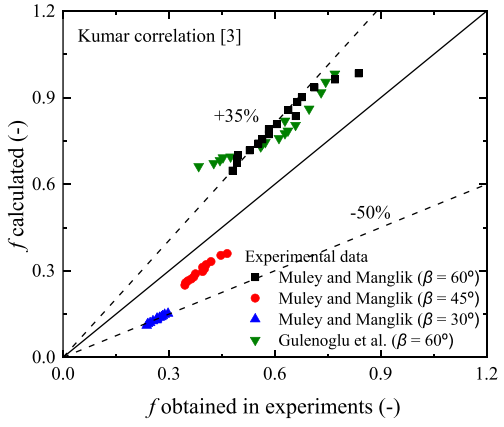


(b) Kumar correlation

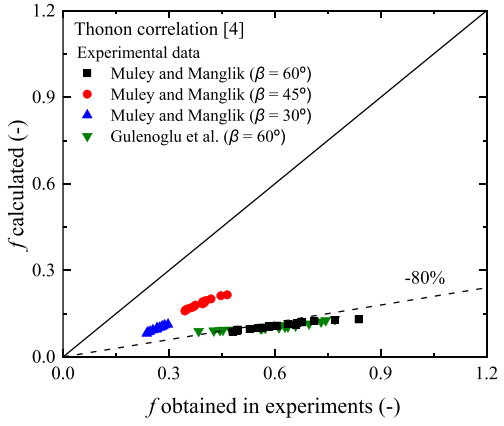


(c) Thonon correlation

**Fig. 6.** Evaluation of correlations for single-phase wall friction factor.

adopted for the prediction of the boiling. Therefore, it was confirmed that the developed code was working reasonably.

## 3. Analysis of CPHE SG

The performances of the rectangular and disk CPHE SGs for the BANDI-60 [15] operating conditions were assessed using the developed one-dimensional analysis code. In this analysis, to investigate the shape effect of the CPHEs, the same heat transfer area and corrugation shape were applied to the two CPHE designs. The coolant volume per channel of the two CPHEs remains same because of the same heat transfer area and corrugation shape. The ratio of the axial length and width of the rectangular CPHE ($L/W$) was determined to be three by following the typical CPHE design. The average flow cross-sectional area of the rectangular CPHE was smaller than that of the disk CPHE. To observe the chevron angle effect, the chevron angle was changed from 30° to 60° in the calculation. The detailed geometrical conditions of both CPHEs are summarized in Table 9.

From the analysis of the node size effect, it was found that the node size effect was negligible if the number of nodes exceeds 92 and 161 for the chevron angle of 30° and 60°, respectively. The node conditions for each CPHE in this analysis are listed in Table 10.

Conventional nuclear power plants use once-through or recirculation SGs. The thermodynamic quality at the exit of the secondary heat transfer region ($x_{2ry.out}$) in the once-through SG is greater than 1.0, whereas the $x_{2ry.out}$ in the recirculation SG is 0.1–0.4. To cover the $x_{2ry.out}$ conditions for the two SGs, the analysis was performed within the $x_{2ry.out}$ range of 0.0–1.0. For this, the mass flow rate of the feedwater at the secondary side changed according to the expected nominal primary mass flow rate of the BANDI-60. The nominal mass flow rate at the primary side was estimated to be 936 kg/s, and the number of channels consisting of each side of the SG for the BANDI-60 was assumed to be 1000. Accordingly, 0.936 kg/s of water ($\dot{m}_{1ry}$) flowed through each channel of the primary side. In this analysis, the feedwater mass flow rate ($\dot{m}_{2ry}$) of each channel for the secondary side was changed from 0.11 kg/s to 1.84 kg/s. Accordingly, the mass flux ($\overline{G}_{2ry}$) ranges in rectangular and disk CPHEs were 85.9–1438.0 kg/m$^2$s and 45.3–757.2 kg/m$^2$s, respectively. In addition, the temperature and pressure at the inlet of the primary side, the pressure at the outlet of the secondary side, and the temperature at the inlet of the secondary side were considered as boundary conditions. The analysis was performed within the following ranges: $1.50 \times 10^3 \leq Re \leq 5.01 \times 10^4$, $2.89 \times 10^{-1} \leq Re_g \leq 1.64 \times 10^4$, $4.77 \leq Bd \leq 8.74$, and $6.33 \times 10^{-6} \leq Bo \leq 3.83 \times 10^{-3}$.

The characteristics of the CPHE SGs in terms of pressure loss, instability, and total heat transfer rate were investigated. First, a parametric analysis of the irreversible pressure loss due to friction and the form losses in the primary side of both CPHEs was attempted. As shown in Fig. 10, the pressure loss increased with the

**Table 4**
RMSE of correlations for single-phase wall friction factor.

| | RMSE (−) | | |
|---|---|---|---|
| Experiments | Muley and Manglik | Kumar | Thonon |
| Muley and Manglik ($\beta = 60°$) | 0.051 | 0.333 | 0.822 |
| Muley and Manglik ($\beta = 45°$) | 0.026 | 0.237 | 0.528 |
| Muley and Manglik ($\beta = 30°$) | 0.041 | 0.504 | 0.632 |
| Gulenoglu et al. ($\beta = 60°$) | 0.102 | 0.383 | 0.818 |
| Total | 0.065 | 0.372 | 0.728 |

**Table 5**
Applicable ranges of Amalfi correlations.

| Parameter | Range | Parameter | Range |
|---|---|---|---|
| $Nu$ | $2.07–5.29 \times 10^2$ | $\beta^*$ | 0.40–1.00 |
| $We_m$ | $2.67 \times 10^{-2}–1.62 \times 10^2$ | $Re_f$ | $2.34 \times 10^1–5.32 \times 10^3$ |
| $Re_{fo}$ | $4.12 \times 10^1–5.36 \times 10^3$ | $Re_g$ | $7.94–3.45 \times 10^4$ |
| $Re_{go}$ | $1.58 \times 10^3–8.58 \times 10^4$ | $Bd$ | $1.89–7.89 \times 10^1$ |
| $\rho^*$ | $1.91 \times 10^1–1.35 \times 10^3$ | $Bo$ | $2.97 \times 10^{-5}–4.05 \times 10^{-3}$ |

**Table 6**
Database for boiling experiments.

| Author | Working fluid | Geometry | Experiment condition | |
|---|---|---|---|---|
| Hsieh et al. [10] | R410a | $L = 450$ mm<br>$W = 120$ mm<br>$\beta = 60^\circ$ $b = 2.9$ mm<br>$p = 10$ mm | $q'' = 10–20$ kW/m$^2$<br>$x = 0.07–0.87$<br>$P_{sat} = 1.08–1.25$ MPa<br>$G = 50–100$ kg/m$^2$s | $Pr = 2.29–2.31$<br>$Re_{fo} = 1.87 \times 10^3–3.98 \times 10^3$<br>$Re_{go} = 2.06 \times 10^4–4.21 \times 10^4$<br>$Re_f = 2.66 \times 10^2–3.63 \times 10^3$<br>$Re_g = 1.60 \times 10^3–3.42 \times 10^4$<br>$We_m = 4.88–1.42 \times 10^2$<br>$\rho^* = 2.28 \times 10^1–2.71 \times 10^1$<br>$Bd = 4.12 \times 10^1–4.45 \times 10^1$<br>$Bo = 4.79 \times 10^{-4}–1.98 \times 10^{-3}$ |
| Yan et al. [9] | R134a | $L = 450$ mm<br>$W = 120$ mm<br>$\beta = 60^\circ$ $b = 2.9$ mm<br>$p = 10$ mm | $q'' = 11–15$ kW/m$^2$<br>$x = 0.10–0.88$<br>$P_{sat} = 0.68–0.80$ MPa<br>$G = 55, 70$ kg/m$^2$s | $Pr = 3.34–3.41$<br>$Re_{fo} = 1.39 \times 10^3–1.90 \times 10^3$<br>$Re_{go} = 2.25 \times 10^4–2.92 \times 10^4$<br>$Re_f = 1.69 \times 10^2–1.61 \times 10^3$<br>$Re_g = 2.82 \times 10^3–2.51 \times 10^4$<br>$We_m = 8.68–7.90 \times 10^1$<br>$\rho^* = 3.03 \times 10^1–3.67 \times 10^1$<br>$Bd = 3.46 \times 10^1–3.72 \times 10^1$<br>$Bo = 8.86 \times 10^{-4}–1.59 \times 10^{-3}$ |
| Han et al. [5] | R410a | $L = 476$ mm<br>$W = 115$ mm<br>$\beta = 45, 55, 70^\circ$ $b = 2.15$ mm<br>$p = 4.9, 5.2, 7.0$ mm | $q'' = 2.5–8.5$ kW/m$^2$<br>$x = 0.15–0.95$<br>$P_{sat} = 0.93–1.26$ MPa<br>$G = 13–34$ kg/m$^2$s | $Pr = 2.29–2.34$<br>$Re_{fo} = 5.53 \times 10^2–7.18 \times 10^2$<br>$Re_{go} = 6.45 \times 10^3–7.73 \times 10^3$<br>$Re_f = 3.23 \times 10^1–5.81 \times 10^2$<br>$Re_g = 1.19 \times 10^3–7.34 \times 10^3$<br>$We_m = 1.55–8.46$<br>$\rho^* = 2.26 \times 10^1–3.21 \times 10^1$<br>$Bd = 1.30 \times 10^1–1.99 \times 10^1$<br>$Bo = 9.47 \times 10^{-4}–1.01 \times 10^{-3}$ |
| Khan et al. [6–8] | Ammonia | $L = 565$ mm<br>$W = 185$ mm<br>$\beta = 30, 45, 60^\circ$ $b = 2.2$ mm<br>$p = 6.25$ mm | $q'' = 21–44$ kW/m$^2$<br>$x = 0.5–0.9$<br>$P_{sat} = 0.15–0.40$ MPa<br>$G = 5.5, 6.5, 8.5$ kg/m$^2$s | $Pr = 1.47–1.78$<br>$Re_{fo} = 1.33 \times 10^2–2.02 \times 10^2$<br>$Re_{go} = 3.29 \times 10^3–4.09 \times 10^3$<br>$Re_f = 7.21 \times 10^1–1.61 \times 10^2$<br>$Re_g = 6.44 \times 10^2–1.75 \times 10^3$<br>$We_m = 0.44–2.76$<br>$\rho^* = 1.99 \times 10^2–5.18 \times 10^2$<br>$Bd = 2.48–8.93$<br>$Bo = 1.95 \times 10^{-3}–6.48 \times 10^{-3}$ |

chevron angle, regardless of the CPHE type. However, the pressure loss in the rectangular CPHE was greater than that in the disk CPHE under the same flow conditions. Because the flow cross-sectional area of the rectangular CPHE was smaller than that of the disk CPHE, the mass flux in the rectangular CPHE was higher. The high mass flux resulted in a large pressure loss per unit length. In addition, the channel length of the rectangular CPHE was greater than that of the disk CPHE. Therefore, the pressure loss of the primary side of the disk CPHE was smaller than that of the rectangular.

The $x_{2ry.out}$ and total pressure change on the secondary side according to the secondary mass flux and chevron angle were evaluated. As shown in Fig. 11, $x_{2ry.out}$ increased as the mass flux decreased in both CPHEs. On the other hand, the tendencies of the total pressure change differed according to the CPHE type. In the rectangular CPHE, the total pressure change varied along the N curve as the mass flux decreased from the onset of boiling (ONB) points. In contrast, in the disk CPHE, the total pressure change follows parabolic shapes as the mass flux decreases. Furthermore, a reverse gradient of the total pressure change to the mass flux was observed. This indicated the possibility of Ledinegg instability [19] occurring on the secondary side of both CPHEs. The reverse gradients were the smallest at a chevron angle of 45° and the largest at a chevron angle of 30°, regardless of the CPHE type in the present analysis.

The pressures calculated at a chevron angle of 30° were analyzed in detail to identify the pressure terms causing the reverse gradient pressure change. The total pressure change consists of the reversible pressure changes due to acceleration and gravitation and the irreversible pressure change due to friction and form losses. As shown in Fig. 12, the acceleration term was much smaller than the other terms, and thus, the effect of acceleration on the instability can be negligible. The gravitational pressure change showed a positive gradient to the mass flux; thus, it contributed to stabilizing the system. However, the pressure change due to friction and form losses had a reverse gradient, and it was approximately 6.4 times larger on average than the gravitation term. Therefore, the behavior of pressure change by friction and form losses governed the instability of the CPHE SG.

The reverse gradient of pressure change due to friction and form losses is related to the behavior of the two-phase flow pressure loss, such as the boiling flow. In the two-phase flow, the pressure loss increased owing to the interfacial friction due to the velocity difference between the liquid and gas. In general, the frictional pressure loss decreased with a decrease in the mass flux according to $\Delta P_{loss} \sim f \frac{L}{d} \frac{G^2}{2\rho}$. However, the boiling region in the channel increased when the mass flux decreased under the given conditions. Therefore, the frictional loss increased despite a decrease in the mass flux owing to the boiling flow.

To avoid the Ledinegg instability of the CPHE SGs, the operating conditions and design of SGs should be determined by considering the pressure change. From the present analysis, the reverse gradients of the total pressure changes were observed in the conditions where $x_{2ry.out}$ was less than 0.16 and 0.11, respectively, in rectangular and disk CPHEs. Accordingly, the instability would not occur in the once-through SG because $x_{2ry.out}$ is higher than 1.0. On the contrary, the recirculation SG, in which $x_{2ry.out}$ is 0.1–0.4, should be designed at an optimal chevron angle, such as 45°, to prevent Ledinegg instability. In addition, the rectangular or disk CPHE SG should be operated under conditions in which the mass flux is less than 552.2 kg/m$^2$s and 409.4 kg/m$^2$s in the present CPHE design.

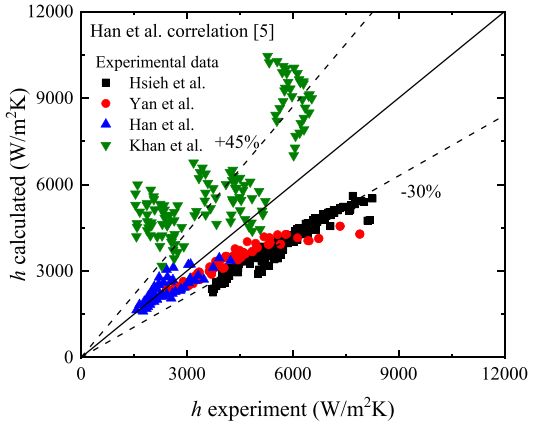


(a) Han et al. correlation

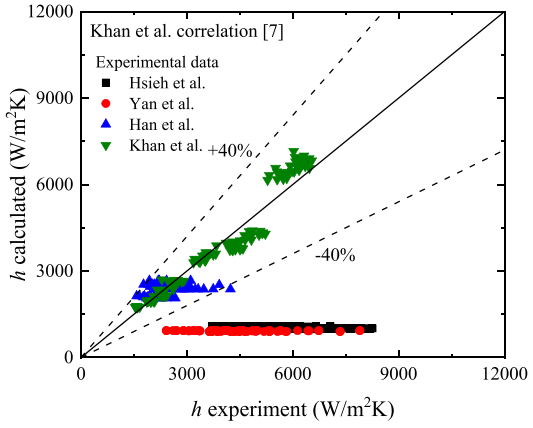


(b) Khan et al. correlation

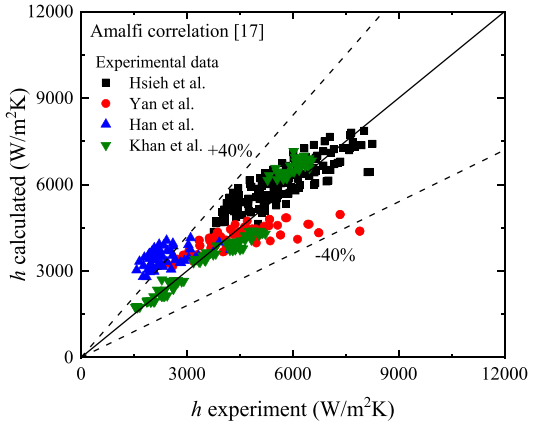


(c) Amalfi correlation

**Fig. 7.** Evaluation of boiling heat transfer correlations.

The total heat transfer rates with respect to the secondary mass flux and chevron angle were investigated under the conditions in which Ledinegg instability did not occur. As shown in Fig. 13, the total heat transfer rates of the two CPHE types increased with the mass flux or chevron angle. In addition, the heat transfer performance of the disk CPHE was better than that of the rectangular CPHE under all mass flux conditions. At the chevron angle of 45°, the heat transfer rate of rectangular CPHE having a mass flux of

**Table 7**
RMSE of correlations for boiling heat transfer.

| | RMSE (−) | | |
|---|---|---|---|
| Experiments | Han et al. | Khan et al. | Amalfi |
| Hsieh et al. | 0.310 | 0.809 | 0.135 |
| Yan et al. | 0.224 | 0.780 | 0.177 |
| Han et al. | 0.125 | 0.210 | 0.562 |
| Khan et al. | 0.916 | 0.094 | 0.094 |
| Total | 0.549 | 0.612 | 0.235 |

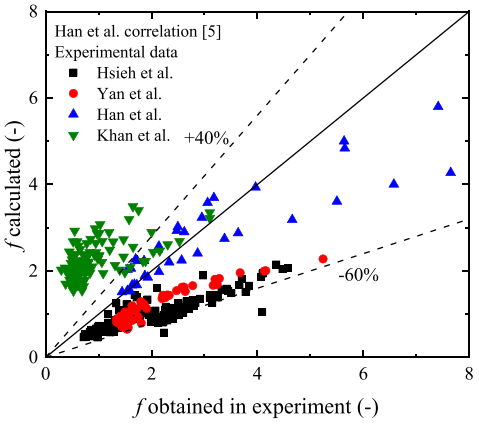


(a) Han et al. correlation

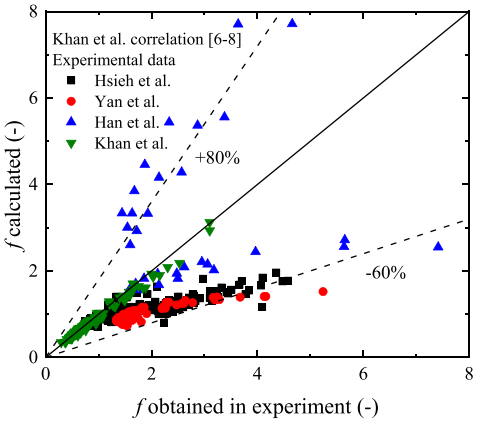


(b) Khan et al. correlation

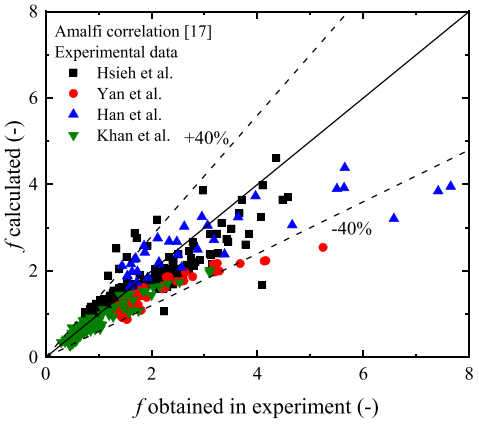


(c) Amalfi correlation

**Fig. 8.** Evaluation of wall friction factor correlations in boiling region.

**Table 8**
RMSE of correlations for boiling wall friction factor.

| | RMSE (−) | | |
|---|---|---|---|
| Experiments | Han et al. | Khan et al. | Amalfi |
| Hsieh et al. | 0.477 | 0.379 | 0.217 |
| Yan et al. | 0.420 | 0.449 | 0.269 |
| Han et al. | 0.201 | 0.706 | 0.261 |
| Khan et al. | 2.269 | 0.070 | 0.215 |
| Total | 1.258 | 0.386 | 0.231 |

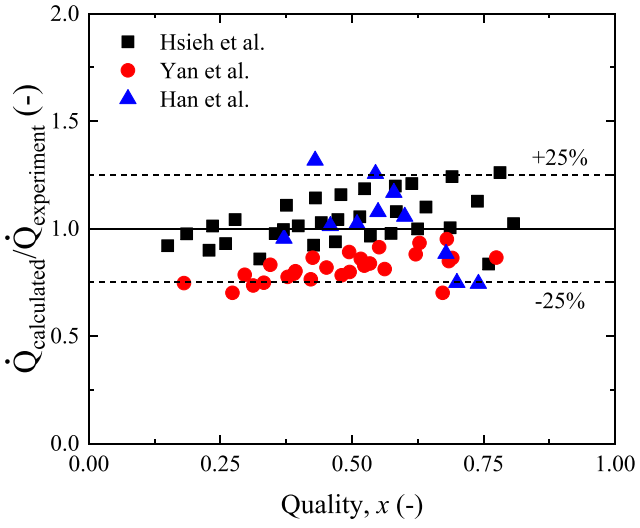


**Fig. 9.** Validation of analysis code for CPHE concerning heat transfer rate.

**Table 9**
Geometrical conditions of CPHEs for analysis.

| | Rectangular | Disk |
|---|---|---|
| Width($W$) or Diameter($d_{disk}$) | 0.640 m | 1.360 m |
| Length ($L$) | 1.916 m | 1.0 m |
| Flow cross-sectional area ($A_{CS}$) | $1.28 \times 10^{-3}$ m$^2$ | $2.43 \times 10^{-3}$ m$^2$ |
| Chevron angle ($\beta$) | 30°, 45°, 60° | |
| Pitch ($\lambda$) | 10 mm | |
| Height of corrugation ($b$) | 2 mm | |
| Thickness ($t$) | 1.5 mm | |
| Materials | SUS 304 | |

**Table 10**
Calculation node for each CPHE.

| Chevron angle ($\beta$) | Size of nodes ($l$) | The number of nodes ($n$) | |
|---|---|---|---|
| | | Rectangular | Disk |
| 30° | 8.7 mm | 221 | 115 |
| 45° | 7.1 mm | 271 | 141 |
| 60° | 5.0 mm | 383 | 201 |

552.2 kg/m$^2$s was 247.0 kW, whereas that of disk CPHE having a mass flux of 409.4 kg/m$^2$s was 322.7 kW. Therefore, the maximum heat transfer rate of the disk CPHE was 30.6% greater than that of the rectangular CPHE under the operating conditions avoiding Ledinegg instability.

To investigate the heat transfer characteristics of the two CPHEs, the thermodynamic quality of the secondary side ($x_{2ry.}$) along the flow direction was analyzed under the condition where $x_{2ry.out}$ was approximately 1.0 and Ledinegg instability would not occur. The

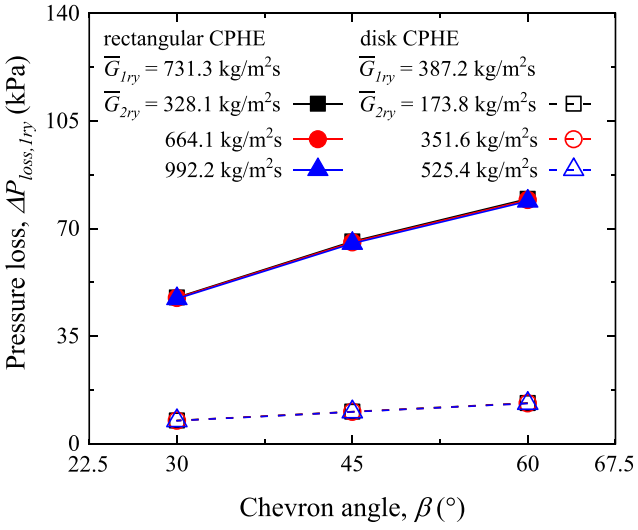


**Fig. 10.** Pressure loss of primary side for chevron angle.

secondary mass flux conditions in the rectangular and disk CPHEs were 82.8 and 43.9 kg/m$^2$s, respectively. The $x$-axis in Fig. 14 represents the dimensionless distance from the inlet. As shown in the figure, the ONB points for the rectangular and disk CPHEs were found at $z/L$ = 0.22 and 0.19, respectively. The $x_{2ry.}$ for the two CPHEs similarly increased in the subcooled liquid region. However, after the ONB points, $x_{2ry.}$ of disk CPHE increased significantly. This implies that the boiling heat transfer in the disk CPHE was more effective than that in the rectangular CPHE.

The greater boiling heat transfer rate of the disk CPHE is due to its total pressure change being smaller than that in the rectangular CPHE. At a given outlet pressure, as a boundary condition in the present analysis, a decrease in the total pressure change reduced the average pressure of the channel. Accordingly, the saturation pressure and saturation temperature were also reduced. Thus, the temperature difference between the wall and secondary fluid increased in the disk CPHE.

## 4. Conclusions

In this study, a one-dimensional analysis code was developed to explore the thermal–hydraulic characteristics of CPHE SGs for small modular reactors. From the analysis, the CPHE SG performance with respect to the chevron angle and mass flux on the secondary side was evaluated using the code. The major results are as follows:

(1) A one-dimensional thermal–hydraulic analysis code for the CPHE SG was developed based on existing thermal–hydraulic models and correlations for the CPHE. For this, constitutive correlations for single and two-phase flows were evaluated against experimental data collected from previous experiments.
(2) The performance of the CPHE SG was analyzed with respect to the chevron angle, secondary mass flux, and CPHE type using the developed code. The present analysis revealed that the primary-side irreversible pressure loss in disk CPHE was lower than that in rectangular CPHE. Because the disk CPHE had a large flow cross-sectional area, the mass flux in the channel of disk CPHE was lower under the same mass flow rate condition.

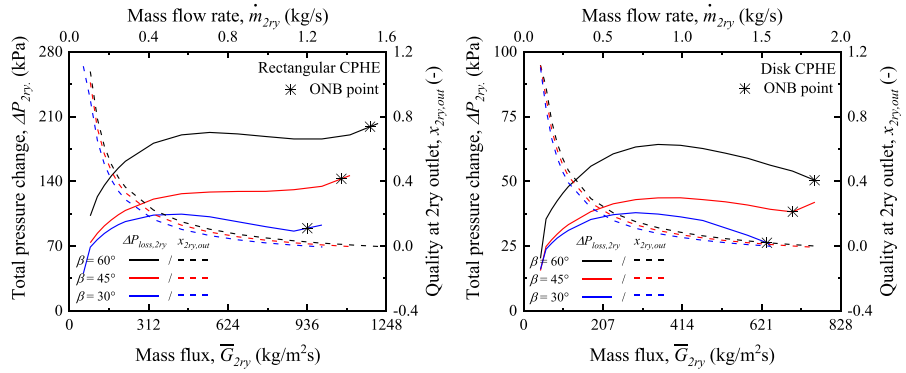


**Fig. 11.** Total pressure change of secondary side.

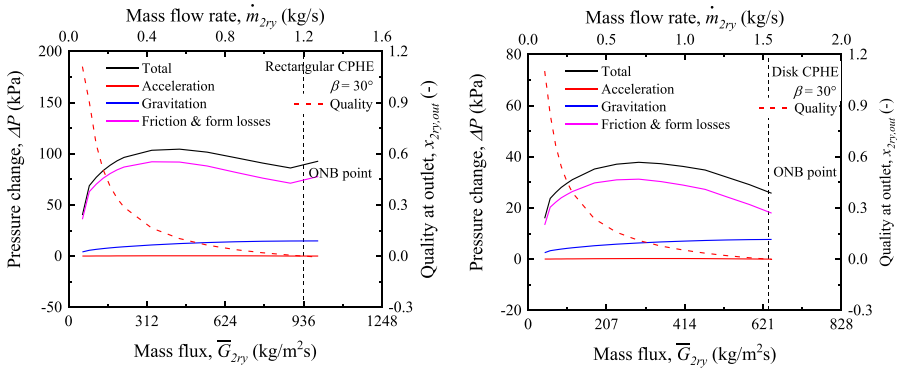


**Fig. 12.** Pressure change curve with respect to mass flux ($\beta = 30°$).

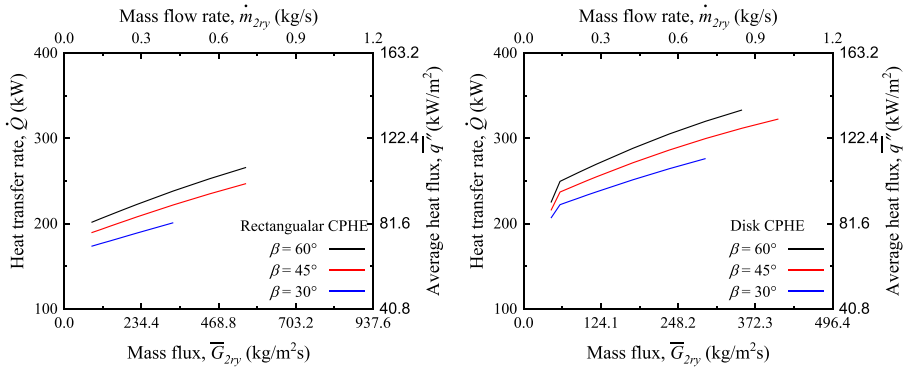


**Fig. 13.** Heat transfer rate to secondary mass flux and chevron angle.

(3) On the secondary side, the reverse gradients of the total pressure change to the mass flux were observed to cause Ledinegg instability in the two-phase flow region. Under the given thermal–hydraulic conditions, it was found that the optimal chevron angle required to avoid instability was 45° in both CPHEs. Furthermore, the operating conditions of the secondary mass flux should be maintained below a mass flux of 552.2 kg/m$^2$s and 409.4 kg/m$^2$s in the present rectangular and disk CPHEs, respectively, to avoid instability.

(4) The heat transfer performances of both CPHEs were similar in the subcooled region, whereas the disk CPHE had a high heat transfer efficiency in the boiling region under a given flow condition. This is attributable to the lower saturation temperature in the disk CPHE than that in the rectangular

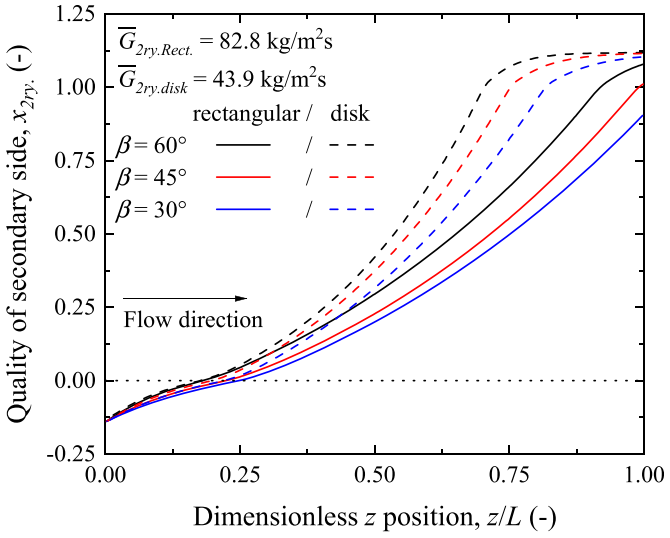


**Fig. 14.** Thermodynamic quality of secondary side along flow direction.

CPHE. The maximum heat transfer rate of disk CPHE was 30.6% higher than that of rectangular CPHE under the conditions where Ledinegg instability did not occur in BANDI-60 SMR.

## Declaration of competing interest

The authors declare that they have no known competing financial interests or personal relationships that could have appeared to influence the work reported in this paper.

## Acknowledgments

This research was supported by the Nuclear Research & Development Program of the National Research Foundation of Korea (NRF) funded by the Ministry of Science, ICT and Future Planning (MSIP) [grant number NRF-2019M2D2A1A03056998], and the Nuclear Safety Research Program through the Korea Foundation of Nuclear Safety (KOFONS) funded by the Nuclear Safety and Security Commission (NSSC), Republic of Korea [grant number 2003001].

## Nomenclature

| | |
|---|---|
| $A_{CS}$ | Flow cross-section ($m^2$) |
| $A_{HT}$ | Heat transfer area ($m^2$) |
| $b$ | Height of corrugation (m) |
| $Bd$ | Bond number (−) |
| $Bo$ | Boiling number (−) |
| $d$ | Diameter (m) |
| $d_h$ | Hydraulic diameter (m) |
| $f$ | Fanning friction factor (−) |
| $G$ | Mass flux ($kg/m^2s$) |
| $g$ | Gravity acceleration (m/s) |
| $Ge$ | Non-dimensional geometric parameter (−) |
| $h$ | Heat transfer coefficient ($W/m^2K$) |
| $i$ | Enthalpy energy (J) |
| $j$ | Node number (−) |
| $K$ | Form loss coefficient (−) |
| $L$ | Length (m) |
| $l$ | Length of node (m) |
| $\dot{m}$ | Mass flow rate (kg/s) |
| $Nu$ | Nusselt number (−) |
| $P$ | Pressure (kPa) |
| $P_a$ | Accelerational pressure (kPa) |
| $P_g$ | Gravitational pressure (kPa) |
| $Pr$ | Prandtl number (−) |
| $q''$ | Heat flux ($W/m^2$) |
| $\dot{Q}$ | Heat transfer rate (W) |
| $Re$ | Reynolds number (−) |
| $t$ | Thickness of plate (m) |
| $T$ | Temperature (K) |
| $W$ | Width (m) |
| $We$ | Weber number (−) |
| $x$ | Thermodynamic quality (−) |
| $z$ | Flow direction (m) |

*Greek letters*

| | |
|---|---|
| $\beta$ | Chevron angle (°) |
| $\lambda$ | Corrugation pitch (m) |
| $\mu$ | Viscosity (Pa·s) |
| $\rho$ | Density ($kg/m^3$) |
| $\sigma$ | Surface tension (N/m) |
| $\phi$ | Enlargement factor |

*Subscripts*

| | |
|---|---|
| $f$ | Saturated liquid |
| $g$ | Saturated gas |
| $j$ | Node number |
| $m$ | Two-phase mixture |
| $w$ | Wall |
| $1ry$ | Primary side |
| $2ry$ | Secondary side |

## References

[1] A. Muley, R.M. Manglik, Experimental study of turbulent flow heat transfer and pressure drop in a plate heat exchanger with chevron plates, J. Heat Tran. 121 (1999) 110–117, https://doi.org/10.1115/1.2825923.
[2] C. Gulenoglu, F. Akturk, S. Aradag, N. Sezer Uzol, S. Kakac, Experimental comparison of performances of three different plates for gasketed plate heat exchangers, Int. J. Therm. Sci. 75 (2014) 249–256, https://doi.org/10.1016/j.ijthermalsci.2013.06.012.
[3] H. Kumar, The plate heat exchanger: construction and design, in: Inst. Chem. Eng. Symp. Ser., 1984, pp. 1275–1288.
[4] B. Thonon, Design method for plate evaporators and condensers, in: BHR, Gr. Conf. Ser. Publ, Mechanical Engineering Publications Limited, 1995, pp. 37–50.
[5] D.H. Han, K.J. Lee, Y.H. Kim, Experiments on the characteristics of evaporation of R410A in brazed plate heat exchangers with different geometric configurations, Appl. Therm. Eng. 23 (2003) 1209–1225, https://doi.org/10.1016/S1359-4311(03)00061-9.
[6] T.S. Khan, M.S. Khan, M.C. Chyu, Z.H. Ayub, Experimental investigation of evaporation heat transfer and pressure drop of ammonia in a 60° chevron plate heat exchanger, Int. J. Refrig. 35 (2012) 336–348, https://doi.org/10.1016/j.ijrefrig.2011.10.018.
[7] M.S. Khan, T.S. Khan, M.C. Chyu, Z.H. Ayub, Evaporation heat transfer and pressure drop of ammonia in a mixed configuration chevron plate heat exchanger, Int. J. Refrig. 41 (2014) 92–102, https://doi.org/10.1016/j.ijrefrig.2013.12.015.
[8] M.S. Khan, T.S. Khan, M.C. Chyu, Z.H. Ayub, Experimental investigation of evaporation heat transfer and pressure drop of ammonia in a 30° chevron plate heat exchanger, Int. J. Refrig. 35 (2012) 1757–1765, https://doi.org/10.1016/j.ijrefrig.2012.05.019.
[9] Y.Y. Yan, T.F. Lin, Evaporation heat transfer and pressure drop of refrigerant R134a in a plate heat exchanger, J. Heat Tran. 121 (1999) 118–127, https://doi.org/10.1115/1.2825924.
[10] Y.Y. Hsieh, T.F. Lin, Saturated flow boiling heat transfer and pressure drop of refrigerant R-410A in a vertical plate heat exchanger, Int. J. Heat Mass Tran. 45 (2002) 1033–1044, https://doi.org/10.1016/S0017-9310(01)00219-8.
[11] Y.C. Tsai, F.B. Liu, P.T. Shen, Investigations of the pressure drop and flow distribution in a chevron-type plate heat exchanger, Int. Commun. Heat Mass Tran. 36 (2009) 574–578, https://doi.org/10.1016/j.icheatmasstransfer.2009.03.013.
[12] X.H. Han, L.Q. Cui, S.J. Chen, G.M. Chen, Q. Wang, A numerical and experimental study of chevron, corrugated-plate heat exchangers, Int. Commun. Heat Mass Tran. 37 (2010) 1008–1014, https://doi.org/10.1016/j.icheatmasstransfer.2010.06.026.

[13] W. Yoon, J.H. Jeong, Development of a numerical analysis model using a flow network for a plate heat exchanger with consideration of the flow distribution, Int. J. Heat Mass Tran. 112 (2017) 1–17, https://doi.org/10.1016/j.ijheatmasstransfer.2017.04.087.
[14] L.O. Freire, D. Ad De Andrade, On applicability of plate and shell heat exchangers for steam generation in naval PWR, Nucl. Eng. Des. 280 (2014) 619–627, https://doi.org/10.1016/j.nucengdes.2014.09.039.
[15] I.H. Kim, J. Won, T. Bae, K. Yi, H.R. Choi, G.S. Kim, S.K. Lee, S. Kim, C.K. Chung, B.G. Kim, J.T. Seo, B.J. Lee, Development of BANDI-60S for a Floating Nuclear Power Plant, vol. 35, 2019, pp. 24–26.
[16] R.L. Amalfi, F. Vakili-Farahani, J.R. Thome, Flow boiling and frictional pressure gradients in plate heat exchangers. Part 1: review and experimental database, Int. J. Refrig. 61 (2016) 166–184, https://doi.org/10.1016/j.ijrefrig.2015.07.010.
[17] R.L. Amalfi, F. Vakili-Farahani, J.R. Thome, Flow boiling and frictional pressure gradients in plate heat exchangers. Part 2: comparison of literature methods to database and new prediction methods, Int. J. Refrig. 61 (2016) 185–203, https://doi.org/10.1016/j.ijrefrig.2015.07.009.
[18] P.A. Kew, K. Cornwell, Correlations for the prediction of boiling heat transfer in small-diameter channels, Appl. Therm. Eng. 17 (1997) 705–715, https://doi.org/10.1016/S1359-4311(96)00071-3.
[19] S. Kakac, B. Bon, A Review of two-phase flow dynamic instabilities in tube boiling systems, Int. J. Heat Mass Tran. 51 (2008) 399–433, https://doi.org/10.1016/j.ijheatmasstransfer.2007.09.026.